Ab initio nucleon-nucleus elastic scattering with chiral effective field theory uncertainties

R. B. Baker,[1] B. McClung,[1] Ch. Elster,[1] P. Maris,[2] S. P. Weppner,[3] M. Burrows,[4] and G. Popa[1]

[1] *Institute of Nuclear and Particle Physics, and Department of Physics and Astronomy, Ohio University, Athens, OH 45701, USA*
[2] *Department of Physics and Astronomy, Iowa State University, Ames, IA 50011, USA*
[3] *Natural Sciences, Eckerd College, St. Petersburg, FL 33711, USA*
[4] *Department of Physics and Astronomy, Louisiana State University, Baton Rouge, LA 70803, USA*

(Dated: December 4, 2021)

Background: Effective interactions for nucleon-nucleus elastic scattering from first principles require the use of the same nucleon-nucleon interaction in the structure and reaction calculations, and a consistent treatment of the relevant operators at each order.

Purpose: Systematic investigations of the effect of truncation uncertainties of chiral nucleon-nucleon (NN) forces have been carried out for scattering observables in the two- and three-nucleons system as well as for bound state properties of light nuclei. Here we extend this type of study to proton and neutron elastic scattering for ^{16}O and ^{12}C.

Methods: Using the frameworks of the spectator expansion of multiple scattering theory as well as the no-core shell model, we employ one specific chiral interaction from the LENPIC collaboration and consistently calculate the leading order effective nucleon-nucleus interaction up to the third chiral order (N2LO), from which we extract elastic scattering observables. Then we apply pointwise as well as correlated uncertainty quantification for the estimation of the chiral truncation error.

Results: We calculate and analyze proton elastic scattering observables for ^{16}O and neutron elastic scattering observables for ^{12}C between 65 and 185 MeV projectile kinetic energy. We find qualitatively similar results for the chiral truncation uncertainties as in few-body systems, and assess them using similar diagnostic tools. The order-by-order convergence of the scattering observables for ^{16}O and ^{12}C is very reasonable around 100 MeV, while for higher energies the chiral expansion parameter becomes too large for convergence. We also find a nearly perfect correlation between the differential cross section for neutron scattering and the NN Wolfenstein amplitudes for small momentum transfers.

Conclusions: The diagnostic tools for studying order-by-order convergence of a chiral NN interaction in observables in few-body systems can be employed for observables in nucleon-nucleus scattering with only minor modifications provided the momentum scale in the problems is not too large. We also find that the chiral NN interaction on which our study is based on, gives a very good description of differential cross sections as well as spin observables for ^{16}O and ^{12}C as low as 65 MeV projectile energy. In addition, the very forward direction of the neutron differential cross section mirrors the behavior of the NN interaction amazingly well.

arXiv:2112.02442v1 [nucl-th] 4 Dec 2021

I. INTRODUCTION

Elastic scattering of protons or neutrons from stable nuclei has traditionally played an important role in determining phenomenological optical models or testing accuracy and validity of microscopic models thereof. Major progress has been made in the development of nucleon-nucleon (NN) and three-nucleon ($3N$) interactions from chiral effective field theory (see e.g. [1–6]). These, together with the utilization of massively parallel computing resources (e.g., see [7–11]), have placed *ab initio* large-scale simulations at the frontier of nuclear structure and reaction explorations. Among other successful many-body theories, the *ab initio* no-core shell-model (NCSM) approach (see, e.g., [12–15]), has over the last decade taken center stage in the development of microscopic tools for studying the structure of atomic nuclei. The NCSM concept combined with a symmetry-adapted (SA) basis in the *ab initio* SA-NCSM [16] has further expanded the reach to the structure of intermediate-mass nuclei [17]. One path of extending the reach of this successful approach to describing reactions is the construction of *ab initio* effective interactions for e.g. elastic scattering of nucleon from nuclei in the framework based on the spectator expansion [18] of multiple scattering theory. Recently the leading order term in the spectator expansion has been successfully derived and calculated, treating the NN interaction consistently when deriving the effective interaction [19, 20].

The recently developed consistent *ab initio* leading order nucleon-nucleus (NA) effective interaction allows the study of truncation uncertainties of the chiral NN interaction in elastic NA scattering observables. In this work we focus on one specific chiral NN interaction [1, 2] and explore truncation uncertainties for elastic proton scattering from ^{16}O and elastic neutron scattering from ^{12}C in the energy regime from 65 to 185 MeV projectile energy.

The choice of considering elastic scattering from these two nuclei has several motivations. First, we want to study nuclei in which the 0^+ ground state has contributions in the p-shell, one of them being spherical and traditionally

considered closed shell (^{16}O) and one being deformed and open shell (^{12}C). Second, we want to consider nuclei where reactions are not accessible to exact few-body methods, and where the structure calculations are reasonably well converged within the NCSM framework. In addition, experimental information for neutron elastic scattering, specifically differential cross sections in the energy regime relevant for this study, is only available for ^{12}C [21] as lightest measured nucleus.

The study of truncation uncertainties in the chiral NN interaction in scattering observables of the NN system has already been successfully carried out (see e.g. [22–24]) and extended to the nucleon-deuteron (Nd) system [25] as well as to structure observables for light nuclei [15, 26]. In this work we follow the procedures developed in Refs. [23, 24] and extend them to study observables in elastic NA scattering. In Section II we briefly give the most important results given in that work, and point the reader to differences to be considered when going from the NN system to a NA system. In Section III we first consider reaction and total cross sections, for which a pointwise uncertainty quantification is best suited. Then we discuss the observables in elastic scattering which depend on the momentum transfer or equivalently the scattering angle, and apply a correlated uncertainty quantification. We also show that the region of low momentum transfer in the differential cross section for neutron elastic scattering can serve as unique window on the order-by-order contributions of the chiral NN interaction. We conclude in Section IV.

II. THEORETICAL FRAMEWORKS

The fundamental idea for the spectator expansion of multiple scattering theory used to calculate the effective interaction employed in elastic NA scattering is an ordering of the scattering process according to the number of active target nucleons interacting directly with the projectile. In this work we consider the leading order of the spectator expansion. Thus only two active nucleons are considered. For the leading order term being derived and calculated *ab initio* means that the NN interaction for the active pair is considered on the same footing as the NN interaction employed to obtain the ground state wave function and one-body density matrices of the target ground state. Details of the derivation of the leading order term and how the spin structure of the NN interaction is consistently taken into account in the reaction process are given in Refs. [19, 20, 27] and shall not be repeated here. Since the leading order in the spectator expansion considers two nucleons being active in the scattering process, we do not include three-nucleon forces which naturally occur in the chiral expansion starting at next-to-next-to-leading order (N2LO).

For the construction of the leading order effective interaction, neutron-proton and neutron-neutron Wolfenstein amplitudes for a given NN interaction are folded with the nonlocal one-body density matrices computed within the NCSM framework using the same NN interaction as input. The studies in this work are based on the semi-local chiral NN interaction by Epelbaum, Krebs, and Meißner [1, 2] with a local cutoff $R = 1.0$ fm. Since the chiral interaction enters on the same footing in the nonlocal NN amplitudes and one-body density matrices, we can explore the effects of the truncations in the chiral orders of the interactions in a consistent fashion on the observables of elastic NA scattering.

To quantify the truncation uncertainty arising from each order in the chiral EFT in the observables we are following two different approaches. The first is a pointwise approach, which we apply to bulk quantities such as reaction and total cross sections at a specified energy. The second is a correlated approach, which we apply to observables that are functions of the scattering angle (momentum transfer) such as the differential cross section $d\sigma/d\Omega$, the analyzing power A_y, and the spin rotation function $\mathcal{Q}$ at specific energies. In the following subsections we summarize the most important features of both approaches. However, we refer the reader to Refs. [23, 24] for detailed descriptions and derivations.

Motivated by the idea of power counting in a chiral EFT, both approaches assume that a quantity $y(x)$ at a given order k can be factorized as

$$y_k(x) = y_{\mathrm{ref}}(x) \sum_{n=0}^{k} c_n(x) Q^n, \tag{1}$$

where $y_{\mathrm{ref}}(x)$ is a reference value that includes the dimensions of the quantity $y(x)$ and sets the scale of the problem. The $c_n(x)$ are dimensionless coefficients and Q is the dimensionless expansion parameter for the EFT. We note that in chiral EFT there is no term linear in Q, i.e. $c_1 \equiv 0$. Most chiral EFTs are constructed such that

$$Q = \max\left(\frac{p}{\Lambda_b}, \frac{M_\pi}{\Lambda_b}\right), \tag{2}$$

where M_π is the mass of the pion, Λ_b is the breakdown scale for the EFT, and p is the relevant momentum. The chiral NN interaction we employ in this work [2] has a breakdown scale of $\Lambda_b = 600$ MeV. In previous work that

studied observables for the NN [23] and Nd [25] systems, several different choices for the relevant momentum were made. Similar to the previous work in the Nd system, we choose to use the center-of-mass (c.m.) momentum of the nucleon-nucleus system p_{NA}, written as

$$p_{NA}^2 = \frac{E_{\rm lab} A^2 m^2 (E_{\rm lab} + 2m)}{m^2 (A+1)^2 + 2AmE_{\rm lab}}, \tag{3}$$

where m is the nucleon mass, A is the mass number of the target nucleus, and $E_{\rm lab}$ is the projectile kinetic energy in the laboratory frame. We assess this choice for the expansion parameter in the section discussing our results by calculating the posteriors for Q.

A. Pointwise uncertainty quantification

The pointwise approach starts from Eq. (1) and assumes the quantity of interest y_k is a scalar rather than a functional quantity. This allows to estimate the truncation uncertainty independent of values at nearby x points. This approach is well suited for calculations of reaction and total cross sections, which are calculated for specific values of the projectile kinetic energy $E_{\rm lab}$ without regard to the value at nearby energies. Assuming the expansion parameter Q and a reference scale $y_{\rm ref}$ are known, the pointwise approach uses Eq. (1) and the values y_k at each order to extract the coefficients c_n. Treating these coefficients as independent draws from the same underlying distribution with variance $\bar{c}^2$, and we can assign priors based on these beliefs and use Bayes' theorem to show that the posterior distribution for the full prediction is given as

$$\mathrm{pr}(y|\vec{y}_k, Q) \sim t_\nu \left(y_k, y_{\rm ref}^2 \frac{Q^{2(k+1)}}{1-Q^2} \tau^2 \right). \tag{4}$$

This is a student-t distribution with degrees of freedom ν and scale τ, which gets multiplied by relevant factors in our problem. As many statistical packages have built-in t distributions, confidence intervals corresponding to our truncation uncertainty can be easily calculated using Eq. (4).

B. Correlated uncertainty quantification

The correlated approach also starts from Eq. (1), but treats $y_k(x)$ as a functional quantity, and encodes information about nearby x points through a correlation length ℓ. This approach is well suited for quantities such as the differential cross section, which can be expressed as a function of either the c.m. angle $\theta_{c.m.}$ or equivalently the momentum transfer q. To incorporate information about nearby angles, this approach treats the c_n as independent draws from an underlying Gaussian process $\mathcal{GP}[\mu, \bar{c}^2 r(x, x'; \ell)]$. The Gaussian process (GP) is defined with two inputs: a mean function (here we have assumed it is a constant μ) and a covariance function. Following the example of others [24], we have chosen a squared exponential as our covariance function, which factorizes into the variance in the coefficients $\bar{c}^2$ multiplied by a correlation function $r(x, x'; \ell)$, where ℓ is the correlation length.

The GP approach requires training and testing data in order to estimate the correlation length and subsequently produce reliable truncation uncertainty bands. We divide the results into smaller subsets of training versus testing data to accommodate this and employ the model-checking diagnostics introduced in Ref. [24] to assess the quality of our GP fits. The first check is comparing the true coefficient curves to their corresponding GP emulated curves and assessing if the true curves are properly captured by the emulator. Secondly, we calculate the Mahalanobis distance $D_{\rm MD}^2$, which is a multivariate analog to the idea of calculating the sum of the squared residuals to measure loss. The quantity $D_{\rm MD}^2$ takes into account the correlations our GP builds in. A large value of $D_{\rm MD}^2$ implies the emulator is not reproducing the validation data. Lastly, we also calculate a pivoted Cholesky decomposition $D_{\rm PC}$, which can identify the data that is contributing to a failing $D_{\rm MD}^2$. Patterns in the $D_{\rm PC}$ values when plotted versus index can indicate variances or correlation lengths that have been incorrectly estimated [24]. We also assess the choice of the expansion parameter Q by calculating the marginal posterior for Q and comparing its maximum *a posteriori* (MAP) value with the value attained by using Eqs. (2) and (3). We refer the reader to Eqs. (A49) and (A53) in Ref. [24] for more details.

III. RESULTS AND DISCUSSION

A. Reaction and total cross sections

Reaction and total cross sections are represented by a single number at each projectile energy, and are therefore best suited to apply the pointwise, uncorrelated approach to uncertainty quantification. For proton scattering from ^{16}O we consider the reaction cross section and for neutron scattering from ^{12}C the total cross section. Since the construction of the effective NA interaction requires the folding of a one-body density matrix obtained from NCSM calculations with the NN interaction calculated at the same order of the chiral expansion, we not only have chiral truncation errors but also numerical errors coming from the corresponding NCSM structure calculation.

As examples we choose the reaction cross section of $^{16}\mathrm{O}(p,p)^{16}\mathrm{O}$ at 100 MeV projectile kinetic energy and the total cross section of $^{12}\mathrm{C}(n,n)^{12}\mathrm{C}$ at 95 MeV, and study the effect of the truncation errors in the chiral EFT as well as the numerical uncertainty of the NCSM calculation. For the reaction cross section (Fig. 1(a)), we see the estimated 1σ truncation uncertainty bands are larger than the numerical uncertainty associated with $\hbar\Omega$ at each $N_{\max}$ value. As $N_{\max}$ increases, the range of possible values resulting from changes in $\hbar\Omega$ decreases slightly, but at $N_{\max} = 10$ the truncation uncertainty dominates the overall uncertainty in this quantity.

For the total cross section, the inset of Fig. 1(b) shows a similar behavior of truncation uncertainty versus numerical uncertainty as was shown for the reaction cross section in Fig. 1(a). The total cross section for neutron scattering on ^{12}C has been studied in the experimental literature and we have included those values and error bars in Fig. 1(b). At N2LO, those experimental values fall within the 1σ truncation uncertainty. To estimate higher order effects on σ_{tot}, we have also performed inconsistent calculations in which the NN amplitudes at N3LO or N4LO are used to calculate the effective interaction, but they are combined with the N2LO one-body density matrix in each case. This is indicated in the figure by empty circles at N3LO and N4LO. Including these results in the uncertainty quantification does provide smaller 1σ uncertainty bands, though we note the experimental values will still fall within the 2σ bands.

B. Differential cross section

Next, we consider functional quantities, i.e. observables that depend on the momentum transfer (or equivalently on the scattering angle), and concentrate first on differential cross sections. To estimate the truncation uncertainty in functional quantities, we use the correlated approach which relies on Gaussian processes. The differential cross section divided by the Rutherford cross section is calculated for proton scattering from ^{16}O at various projectile kinetic energies and compared to experimental data as is shown in Fig. 2. These results indicate a strong dependence on the expansion parameter Q at higher energies, as is expected by the tabulated values of Q shown in Table I. Specifically, the truncation uncertainty bands at N2LO for 180 MeV projectile kinetic energy are sufficiently large that the predictive power at that energy is virtually nonexistent. Nonetheless, the increasing agreement with data in the first peak and first minimum as higher orders are included gives the correct trend. Minima in the differential cross section correlate with the size of the target nucleus. It is well known [15] that the nuclear binding energy calculated with the LO of the chiral NN interaction is way too large and correspondingly the radius much too small. Only when going to NLO and N2LO the binding energy as well as the radius move into the vicinity of their experimental values. This insight from structure calculations is corroborated by the calculations in Fig. 2, where with increasing chiral order the calculated first diffraction minimum moves towards smaller angles (momentum transfers) indicating a larger nuclear size.

We further apply the same approach to the differential cross section for neutron scattering from ^{12}C. The calculations are shown in Fig. 3. Here the angular range is chosen to only cover the range for which data are available. Considering both the experimental error bars and the truncation error bars, we see good agreement with the available data. Similar to the proton scattering case, we again see the effect of the large expansion parameter at higher energies, with the truncation error bars remaining large at N2LO.

To assess our choice of the procedure to estimate the expansion parameter, we calculated posteriors for Q given the $^{16}\mathrm{O}(p,p)^{16}\mathrm{O}$ and $^{12}\mathrm{C}(n,n)^{12}\mathrm{C}$ differential cross sections at each energy (Fig. 4). From each of these posteriors, we can extract the maximum *a posteriori* (MAP) value corresponding to the single value best guess for that quantity. Comparing this MAP value with the prescription for Q we have implemented, we can see they are in generally good agreement though there is some freedom to choose smaller or larger Q values. It is worthwhile to note the differential cross sections shown here are truncated such that values corresponding to a momentum transfer q larger than p_{NA} are excluded to alleviate any concerns about it shifting Q to even larger values. In addition, for proton scattering, we excluded the smallest angles in the differential cross section because they are dominated by Rutherford scattering. This was done in order to assess the truncation errors arising solely from the nuclear interaction and achieve good fits for the Gaussian process.

Examples of the Gaussian process diagnostics used to assess our fits for proton and neutron scattering are shown in Figs. 5 and 6, respectively. As previously mentioned, for proton scattering, the Gaussian process ignores small angles when fitting because the effect of Rutherford scattering rapidly alters the correlation length. This behavior yields bad diagnostics, particularly for the Mahalanobis distance $D^2_{\rm MD}$, which increases to unrealistically large values. Choosing to not train or test the GP in that region alleviates those concerns – this is indicated in Fig. 5 by a lack of tick marks at small angles. In contrast, the GP for neutron scattering can be trained and tested on small angles while still yielding realistic values for the $D^2_{\rm MD}$. Unlike the GP applications in NN scattering where $\mu = 0$, we find a small, positive, constant mean μ yields slightly better fits, especially for the pivoted Cholesky decomposition $D_{\rm PC}$. In both Figs. 5 and 6, we used $\mu = 0.5$, which make the $D_{\rm PC}$ values more equally distributed among postive and negative values. If $\mu = 0$ is used instead, the $D_{\rm PC}$ values are noticeably more positive than negative. While this mean value was determined empirically, future work could learn an appropriate mean from the data, much like what was done for the expansion parameter.

C. Analyzing power

Spin observables usually give more detailed insights into the effective NA interaction, since they are ratios between cross sections and absolute magnitudes are divided out. The scattering of a spin-$\frac{1}{2}$ proton from a spin-0 nucleus allows for two independent spin observables, the analyzing power A_y for transverse polarized protons, and the spin rotation function $\mathcal{Q}$ for longitudinal polarized protons.

In this subsection we want to concentrate on A_y for proton scattering from ^{16}O at a selection of laboratory kinetic energies. In Fig. 7 calculations based on LO, NLO, and N2LO in the chiral NN interaction are shown for 65 MeV, 100 MeV, and 135 MeV and compared to available experimental data. Chiral NN interactions only acquire spin-orbit contributions in NLO, which is clearly seen in the middle column in Fig. 7, where the calculations start to follow the structure of the data. We see good agreement between the theoretical results and experimental data at 100 MeV, particularly in forward directions, but observe noticeable differences between theory at N2LO and experimental data at 135 MeV. Connecting this with observations for the differential cross section at higher energies suggests that the chiral interaction we employ for the current study may be best suited to describe experimental scattering results at projectile energies around 100 MeV or lower. To test if this observation is independent of the choice of nucleus, we substitute proton scattering from ^{12}C for the equivalent neutron scattering calculations. In Fig. 8 the analyzing power for proton scattering on ^{12}C at 65 and 122 MeV is shown. Similar to ^{16}O, these results show good agreement at forward angles, with differences between theory and experiment developing at larger angles/higher momentum transfers.

The associated GP diagnostics for the analyzing power in proton scattering from ^{16}O are shown in Fig. 9. The gray dashed line in the coefficient plot, which goes to zero at 0°, indicates we have used the symmetry-constrained GP procedure from Ref. [24]. Since the value of the A_y must be zero at that point, the truncation error bars should also go to zero. All of our plots in Fig. 8 start at 2°, and because the value of the error bars grows rapidly, this effect cannot be seen there. It should be noted that the Mahalanobis distance $D^2_{\rm MD}$ for LO is essentially zero and lies outside the 95% CI represented by the the whiskers on the box plot, indicating that the LO coefficient curve may not be well-captured by the GP. Since the LO result is essentially zero at all angles (momentum transfers), this matches our expectation and others observations [23] that the leading order result may not be informative to our analysis, particularly for spin observables. Lastly, again, the analyzing power required a small nonzero mean ($\mu = 0.3$) to equally distribute the $D_{\rm PC}$ values.

D. Spin rotation function

The spin rotation function $\mathcal{Q}$ is the second, independent spin observable in scattering of protons from spin-0 nuclei. Experimental information for this observable is considerably scarcer, since its determination requires analyzing the polarization of the scattered particles [28]. Fortunately experimental information is available at 65 MeV for proton scattering from ^{16}O and ^{12}C. In Fig. 10 we present our calculations together with the experimental data.

In both cases, the N2LO result with its associated truncation error bars captures most of the data, particularly in more forward directions. We want to point out, that already the NLO calculations follow the general shape of the data. As in the case of the analyzing power, the LO calculation for which the chiral interaction lacks spin-operators shows a zero spin rotation function in forward direction.

The associated GP diagnostics (Fig. 11) illustrate that the coefficient curves for the spin rotation function are more difficult to model than the previous examples, but decent fits can still be obtained. Notably, here, the $D^2_{\rm MD}$ values for each order are more spread out than previous cases, though only the LO value falls outside of the 95% confidence

interval indicated by the whiskers on the box plot. This is similar to the behavior seen for the analyzing power and again may be a reflection of the leading order result not being informative for spin observables. Unlike both the differential cross section and the analyzing power, the pivoted Cholesky decomposition for the spin rotation function did not require the use of a nonzero mean to evenly distribute its points across the x-axis. This may be a reflection of the behavior of the result at each order for this particular interaction – that is, in the case of the differential cross sections and the analyzing powers we have calculated here, the result at each order is almost always larger (more positive) than the result at the previous order. In constrast, the values for the spin rotation function are essentially zero at LO, become negative at NLO, and then become less negative at N2LO. This oscillating behavior between orders may have alleviated the need for a nonzero mean when fitting.

E. Neutron-nucleus scattering in forward direction

The scattering observables and their analysis in terms of the truncation uncertainties coming from the underlying chiral EFT indicate that when looking at small momentum transfer, there seems to be a similar behavior in the convergence pattern as was observed in studies of the NN observables [1, 2, 22]. This is a nontrivial observation, since *a priori* one can not expect that e.g. multiple scattering effects resulting from first solving the integral equation to obtain the Watson potential [29] and then second from solving the Lippmann-Schwinger integral equation do not influence the analysis. Our calculations are based on an *ab initio* effective interaction calculated in the leading of the spectator expansion of a multiple scattering theory [19], in which a one-body nuclear density matrix is folded with NN amplitudes calculated from the same NN force. In the elastic scattering of a proton (neutron) from a spin-0 nucleus the effective interaction contains only two contributions, a spin-independent central potential and a spin-orbit potential. As shown in detail in Refs. [19, 27], the central potential is built by folding the NN Wolfenstein [30] amplitudes A and C with the nuclear density matrix, while the spin-orbit potential contains contributions from the NN Wolfenstein amplitudes C and M. Furthermore, one should note that the amplitude C is zero for zero-momentum transfer, and very small for momentum transfers $q \leq 1$ fm^{-1}. This means that the small momentum region is dominated by the spin-independent components of the neutron-proton (np) and proton-proton (pp) amplitudes A and thus studying the elastic NA differential cross section in this region opens a unique window on specific pieces of the NN interaction.

In order to investigate if there is a direct correlation between the Wolfenstein amplitude A and the differential cross sections for neutron scattering at small momentum transfers, we should consider the order-by-order contributions to the square of A, summed over np and pp contributions. In Fig. 12(a) this quantity is plotted as a function of the momentum transfer in the NN system at the energy entering the neutron-^{12}C scattering (95 MeV), where the result at each order of the chiral expansion is shown. As expected from Refs. [1, 2], the result shows excellent convergence with increasing chiral order. In Fig. 12(b) the differential cross section for neutron scattering from ^{12}C is shown for the same momentum transfer based on the same chiral orders. We note that consistent *ab initio* calculations are only carried out up to N2LO. For the N3LO and N4LO calculations we used the one-body densities obtained in N2LO and folded them with the corresponding NN amplitudes in the higher chiral orders. We expect this inconsistency to have little effect on the differential cross section in forward direction in our investigation, since the main features of the ground state one-body density matrix are already established at the N2LO level. We observe a very similar behavior in the convergence with respect to the chiral order as seen in Fig. 12(a). The qualitative similarities between the two quantities are striking, with the values of both increasing as higher order contributes are included. From N2LO on, the changes induced by N3LO and N4LO contributions are small in comparison.

To explore the connection between these two quantities further, we have plotted them as functions of each other in Fig. 13(a) for momentum transfers $q \leq 0.55$ fm^{-1}. This results in a linear correlation, albeit with slightly differing slopes and y-intercepts. Normalizing for these differences using the same technique as discussed in Ref. [31] and implemented in Refs. [20, 32], in Fig. 13(b) we see these two quantities are strongly correlated with a correlation coefficient of 0.99. This implies that the forward direction in NA scattering provides a direct connection to the underlying NN interaction. We also found that a simliarly good correlation between the squares of the Wolfenstein amplitudes A and the neutron differential cross section exists for energies as low as 65 MeV and as high as 185 MeV. This observation may be useful when attempting to link properties of a NN interaction to its effects in elastic NA observables, even if only in a small range of momentum transfers.

IV. CONCLUSIONS AND OUTLOOK

We have successfully implemented two procedures to quantify the theoretical uncertainties associated with the underlying chiral EFT used to describe *ab initio* nucleon-nucleus elastic scattering. While both procedures have been applied in the NN and Nd systems, we extend their application to the NA system to study proton scattering from ^{16}O

and neutron scattering from ^{12}C at various energies. For both reactions, we have shown that the uncertainty associated with the chiral expansion is larger than the numerical uncertainty associated with the many-body method used to describe the target nucleus. We also have shown that our prescription for estimating the expansion parameter using the nucleon-nucleus center-of-mass momentum is supported by an analysis of the posterior distributions for Q. This places a limit on the energy range where we can apply these tools because as the projectile energies approach 200 MeV, this yields a chiral EFT expansion parameter of approximately one. At energies of about 100 MeV projectile kinetic energy and lower these tools work very well, showing that with increasing chiral order the truncation uncertainty decreases. We also find that the chiral NN interaction we base our studies on [1, 2] agrees very well with experiment at 100 MeV and lower. At energies higher than 100 MeV, the expansion parameter increases and as a result the chiral truncation uncertainties become very large. We also see a deterioration of the agreement of our central values with experiment for those energies. This is somewhat in contrast to previous studies and experiences using different interactions [19, 33, 34] which described NN observables about equally well at energies up to 200 MeV. The systematic study of chiral truncation uncertainties, carried out here for the first time, seems to indicate that *ab initio* effective NA interactions derived from certain chiral EFTs allows for a good description of experiment at energies lower than previously assumed, provided we focus on regions of momentum transfer where the analysis of the EFT truncation uncertainty is valid.

While examining the differential cross sections in forward directions and low momentum transfers, both proton-nucleus and neutron-nucleus reactions yielded useful insights. For proton-nucleus scattering, we saw that the influence of Rutherford scattering can negatively affect the tools used for uncertainty quantification as the effects coming from the nuclear interaction are overwhelmed by contributions from the Coulomb interaction. For neutron-nucleus scattering, we have shown that the forward direction can provide a unique window into the underlying NN interaction. Specifically, we identified a strong correlation between the differential cross section in $^{12}\mathrm{C}(n,n)^{12}\mathrm{C}$ and the NN Wolfenstein amplitude A representing the spin-independent part of the NN interaction at low momentum transfers. Thus, provided there is experimental data for neutron-nucleus scattering at low momentum transfers, this could indicate a new region to examine when assessing a NN interaction.

ACKNOWLEDGMENTS

The authors appreciate the many useful discussions with K. D. Launey. R. B. B. and Ch. E. gratefully acknowledge fruitful discussions with R. J. Furnstahl about quantifying truncation errors in EFTs. Ch. E. acknowledges useful discussions with A. Nogga about the LENPIC chiral NN interactions. This work was performed in part under the auspices of the U. S. Department of Energy under contract Nos. DE-FG02-93ER40756 and DE-SC0018223, and by the U. S. NSF (PHY-1913728). The numerical computations benefited from computing resources provided by the Louisiana Optical Network Initiative and HPC resources provided by LSU, together with resources of the National Energy Research Scientific Computing Center, a U. S. DOE Office of Science User Facility located at Lawrence Berkeley National Laboratory, operated under contract No. DE-AC02-05CH11231.

[1] E. Epelbaum, H. Krebs, and U. G. Meißner, Phys. Rev. Lett. **115**, 122301 (2015), arXiv:1412.4623 [nucl-th].
[2] E. Epelbaum, H. Krebs, and U. G. Meißner, Eur. Phys. J. A **51**, 53 (2015), arXiv:1412.0142 [nucl-th].
[3] P. Reinert, H. Krebs, and E. Epelbaum, Eur. Phys. J. A **54**, 86 (2018), arXiv:1711.08821 [nucl-th].
[4] E. Epelbaum, H. Krebs, and P. Reinert, Front. in Phys. **8**, 98 (2020), arXiv:1911.11875 [nucl-th].
[5] R. Machleidt and D. R. Entem, Phys. Rept. **503**, 1 (2011), arXiv:1105.2919 [nucl-th].
[6] D. R. Entem, R. Machleidt, and Y. Nosyk, Phys. Rev. C **96**, 024004 (2017), arXiv:1703.05454 [nucl-th].
[7] D. Langr, T. Dytrych, J. P. Draayer, K. D. Launey, and P. Tvrdik, Comp. Phys. Comm. **244**, 442 (2019).
[8] D. Langr, T. Dytrych, K. D. Launey, and J. P. Draayer, The Int. J. of High Performance Computing Applications **33**, 522 (2019).
[9] M. Shao, H. M. Aktulga, C. Yang, E. G. Ng, P. Maris, and J. P. Vary, Comp. Phys. Comm. **222**, 1 (2018), arXiv:1609.01689 [nucl-th].
[10] H. M. Aktulga, C. Yang, E. G. Ng, P. Maris, and J. P. Vary, Concurrency and Computation: Practice and Experience **26**, 2631 (2014).
[11] M. Jung, E. H. Wilson, III, W. Choi, J. Shalf, H. M. Aktulga, C. Yang, E. Saule, U. V. Catalyurek, and M. Kandemir, in Proceedings of the International Conference on High Performance Computing, Networking, Storage and Analysis, SC '13 (ACM, New York, NY, USA, 2013) pp. 75:1–75:11.
[12] P. Navratil, J. P. Vary, and B. R. Barrett, Phys. Rev. Lett. **84**, 5728 (2000), arXiv:nucl-th/0004058 [nucl-th].
[13] R. Roth and P. Navratil, Phys. Rev. Lett. **99**, 092501 (2007), arXiv:0705.4069 [nucl-th].
[14] B. Barrett, P. Navrátil, and J. Vary, Prog. Part. Nucl. Phys. **69**, 131 (2013).

[15] S. Binder, A. Calci, E. Epelbaum, R. J. Furnstahl, J. Golak, K. Hebeler, T. Hüther, H. Kamada, H. Krebs, P. Maris, Ulf-G. Meißner, A. Nogga, R. Roth, R. Skibiński, K. Topolnicki, J. P. Vary, K. Vobig, and H. Witała (LENPIC Collaboration), Phys. Rev. C **98**, 014002 (2018), arXiv:1802.08584 [nucl-th].

[16] K. D. Launey, T. Dytrych, and J. P. Draayer, Prog. Part. Nucl. Phys. **89**, 101 (2016), arXiv:1612.04298 [nucl-th].

[17] T. Dytrych, K. D. Launey, J. P. Draayer, D. J. Rowe, J. L. Wood, G. Rosensteel, C. Bahri, D. Langr, and R. B. Baker, Phys. Rev. Lett. **124**, 042501 (2020), arXiv:1810.05757 [nucl-th].

[18] E. R. Siciliano and R. M. Thaler, Phys. Rev. **C16**, 1322 (1977).

[19] M. Burrows, R. B. Baker, Ch. Elster, S. P. Weppner, K. D. Launey, P. Maris, and G. Popa, Phys. Rev. C **102**, 034606 (2020), arXiv:2005.00111 [nucl-th].

[20] R. B. Baker, M. Burrows, Ch. Elster, K. D. Launey, P. Maris, G. Popa, and S. P. Weppner, Phys. Rev. C **103**, 054314 (2021), arXiv:2102.01025 [nucl-th].

[21] J. H. Osborne, F. P. Brady, J. L. Romero, J. L. Ullmann, D. S. Sorenson, A. Ling, N. S. P. King, R. C. Haight, J. Rapaport, R. W. Finlay, E. Bauge, J. P. Delaroche, and A. J. Koning, Phys. Rev. C **70**, 054613 (2004).

[22] R. J. Furnstahl, N. Klco, D. R. Phillips, and S. Wesolowski, Phys. Rev. C **92**, 024005 (2015), arXiv:1506.01343 [nucl-th].

[23] J. A. Melendez, S. Wesolowski, and R. J. Furnstahl, Phys. Rev. C **96**, 024003 (2017), arXiv:1704.03308 [nucl-th].

[24] J. A. Melendez, R. J. Furnstahl, D. R. Phillips, M. T. Pratola, and S. Wesolowski, Phys. Rev. C **100**, 044001 (2019), arXiv:1904.10581 [nucl-th].

[25] E. Epelbaum, J. Golak, K. Hebeler, H. Kamada, H. Krebs, Ulf-G. Meißner, A. Nogga, P. Reinert, R. Skibiński, K. Topolnicki, Y. Volkotrub, and H. Witała, Eur. Phys. J. A **56**, 92 (2020), arXiv:1907.03608 [nucl-th].

[26] P. Maris, E. Epelbaum, R. J. Furnstahl, J. Golak, K. Hebeler, T. Hüther, H. Kamada, H. Krebs, Ulf-G. Meißner, J. A. Melendez, A. Nogga, P. Reinert, R. Roth, R. Skibiński, V. Soloviov, K. Topolnicki, J. P. Vary, Yu. Volkotrub, H. Witała, and T. Wolfgruber, Phys. Rev. C **103**, 054001 (2021), arXiv:2012.12396 [nucl-th].

[27] M. Burrows, Ab Initio Leading Order Effective Interactions for Scattering of Nucleons from Light Nuclei, Ph.D. thesis, Ohio University (2020).

[28] L. Wolfenstein, Phys. Rev. **96**, 1654 (1954).

[29] C. R. Chinn, Ch. Elster, and R. M. Thaler, Phys. Rev. C **47**, 2242 (1993).

[30] L. Wolfenstein and J. Ashkin, Phys. Rev. **85**, 947 (1952).

[31] K. D. Launey, S. Sarbadhicary, T. Dytrych, and J. P. Draayer, Comp. Phys. Comm. **185**, 254 (2014).

[32] M. Burrows, Ch. Elster, S. P. Weppner, K. D. Launey, P. Maris, A. Nogga, and G. Popa, Phys. Rev. C **99**, 044603 (2019), arXiv:1810.06442 [nucl-th].

[33] S. Weppner, Ch. Elster, and D. Huber, Phys. Rev. C **57**, 1378 (1998), arXiv:nucl-th/9712001.

[34] Ch. Elster, S. P. Weppner, and C. R. Chinn, Phys. Rev. C **56**, 2080 (1997).

[35] R. W. Finlay, W. P. Abfalterer, G. Fink, E. Montei, T. Adami, P. W. Lisowski, G. L. Morgan, and R. C. Haight, Phys. Rev. C **47**, 237 (1993).

[36] C. D. Pruitt, R. J. Charity, L. G. Sobotka, J. M. Elson, D. E. M. Hoff, K. W. Brown, M. C. Atkinson, W. H. Dickhoff, H. Y. Lee, M. Devlin, N. Fotiades, and S. Mosby, Phys. Rev. C **102**, 034601 (2020), arXiv:2006.00024 [nucl-ex].

[37] H. Sakaguchi, M. Nakamura, K. Hatanaka, A. Goto, T. Noro, F. Ohtani, H. Sakamoto, and S. Kobayashi, Phys. Lett. B **89**, 40 (1979).

[38] H. Seifert, Energy Dependence of the Effective Interaction for Nucleon-Nucleus Scattering, Ph.D. thesis, University of Maryland (1990).

[39] J. J. Kelly, W. Bertozzi, T. N. Buti, J. M. Finn, F. W. Hersman, C. Hyde-Wright, M. V. Hynes, M. A. Kovash, B. Murdock, B. E. Norum, B. Pugh, F. N. Rad, A. D. Bacher, G. T. Emery, C. C. Foster, W. P. Jones, D. W. Miller, B. L. Berman, W. G. Love, J. A. Carr, and F. Petrovich, Phys. Rev. C **39**, 1222 (1989).

[40] J. J. Kelly, J. M. Finn, W. Bertozzi, T. N. Buti, F. W. Hersman, C. Hyde-Wright, M. V. Hynes, M. A. Kovash, B. Murdock, P. Ulmer, A. D. Bacher, G. T. Emery, C. C. Foster, W. P. Jones, D. W. Miller, and B. L. Berman, Phys. Rev. C **41**, 2504 (1990).

[41] M. Ieiri, H. Sakaguchi, M. Nakamura, H. Sakamoto, H. Ogawa, M. Yosol, T. Ichihara, N. Isshiki, Y. Takeuchi, H. Togawa, T. Tsutsumi, S. Hirata, T. Nakano, S. Kobayashi, T. Noro, and H. Ikegami, Nucl. Instrum. Methods Phys. Res. A **257**, 253 (1987).

[42] H. O. Meyer, P. Schwandt, W. W. Jacobs, and J. R. Hall, Phys. Rev. C **27**, 459 (1983).

[43] H. Sakaguchi, M. Yosoi, M. Nakamura, T. Noro, H. Sakamoto, T. Ichihara, M. Ieiri, Y. Takeuchi, H. Togawa, T. T., H. Ikegami, and S. Kobayashi, J. Phys. Soc. Japan Suppl. **55**, 61 (1986).

[44] R. Machleidt, Phys. Rev. C **63**, 024001 (2001), arXiv:nucl-th/0006014 [nucl-th].

^{16}O			^{12}C		
$E_{\rm lab}$ (MeV)	p_{NA} (MeV)	Q	$E_{\rm lab}$ (MeV)	p_{NA} (MeV)	Q
65	333.075	0.55	65	326.319	0.54
100	415.984	0.69	95	396.645	0.66
135	486.598	0.81	155	512.013	0.85
180	566.646	0.94	185	562.242	0.93

TABLE I. Center-of-mass momentum p_{NA} and associated expansion parameter Q for various energies in elastic nucleon scattering from ^{16}O and ^{12}C. Values for Q are calculated assuming $\Lambda_b = 600$ MeV.

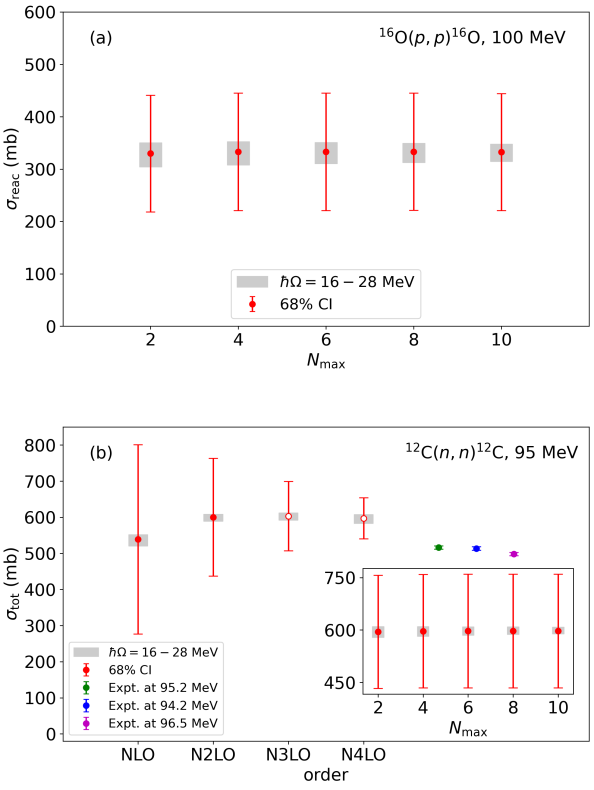


FIG. 1. (a) Reaction cross section for ^{16}O$(p,p)^{16}$O for 100 MeV at N2LO as a function of $N_{\rm max}$. The gray shaded regions show variations in $\hbar\Omega$. The red error bars are the 68% CIs resulting from using the pointwise approach on the LO, NLO, and N2LO results at $\hbar\Omega = 20$ MeV with $Q = 0.69$ and $y_{\rm ref}$ = N2LO. (b) Total cross section for ^{12}C$(n,n)^{12}$C for 95 MeV as a function of order compared to experimental data. The experimental value at 95.2 MeV is from Ref. [35] and the other two experimental values are from Ref. [36]. The inset shows the total cross section as a function of $N_{\rm max}$. See text for further discussion.

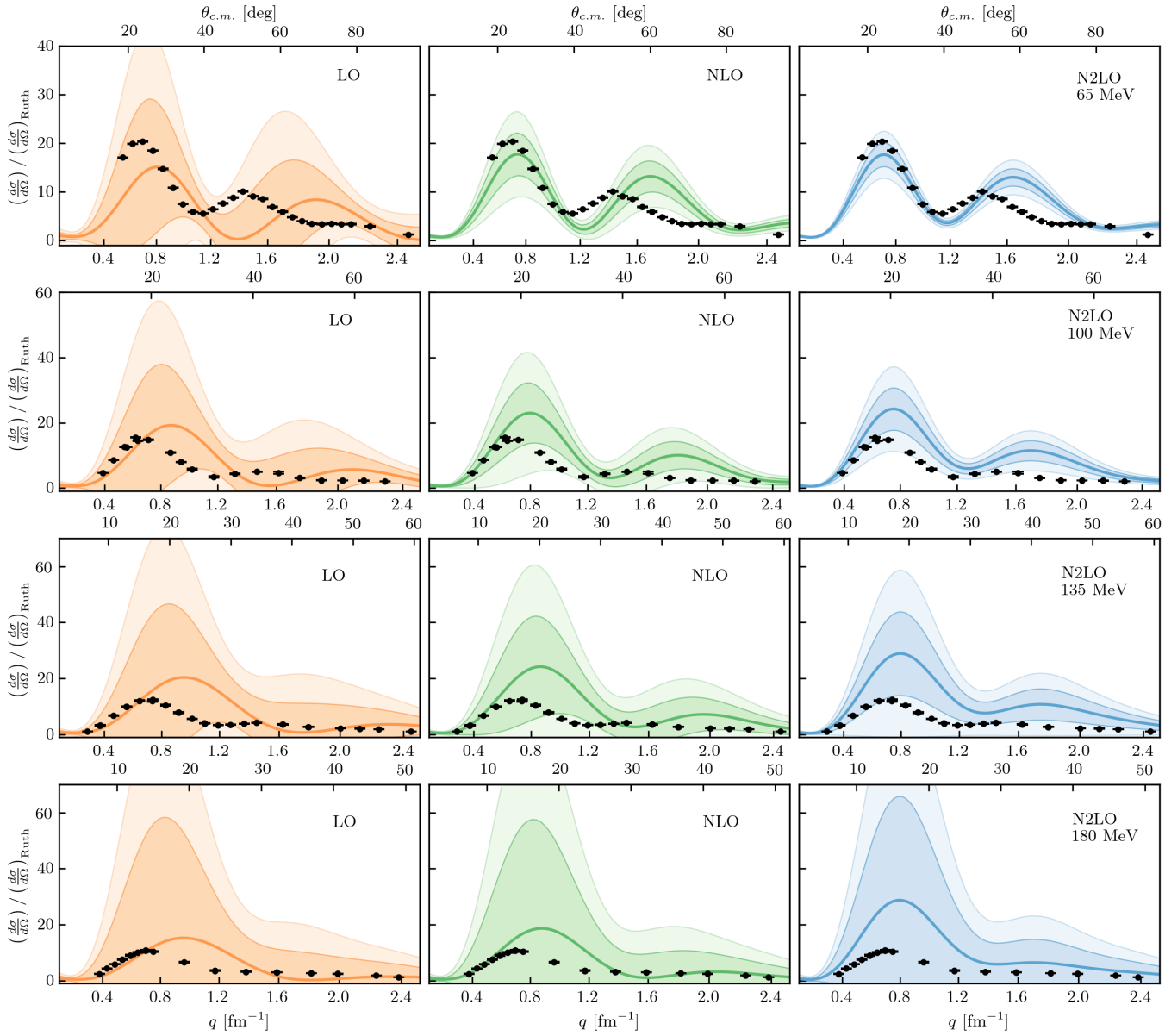


FIG. 2. Differential cross section divided by Rutherford at LO (left column), NLO (middle column), and N2LO (right column) with corresponding 1σ (darker bands) and 2σ (lighter bands) error bands for $^{16}\mathrm{O}(p,p)^{16}\mathrm{O}$ at (first row) 65 MeV, (second row) 100 MeV, (third row) 135 MeV, and (fourth row) 180 MeV. Black dots are experimental data from Refs. [37] (65 MeV), [38] (100 MeV), [39] (135 MeV), and [40] (180 MeV). See text for further discussion.

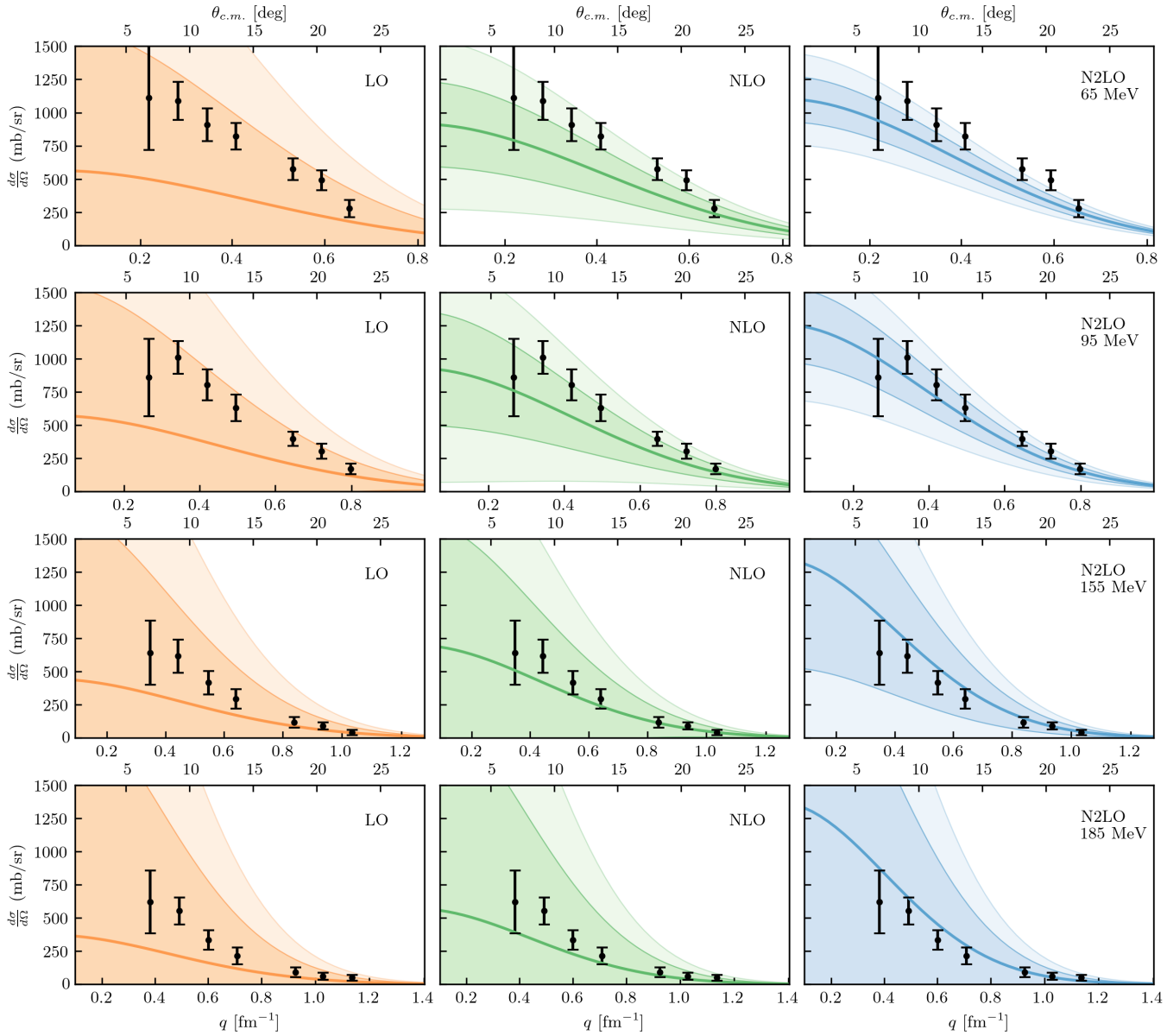


FIG. 3. Differential cross section at LO (left column), NLO (middle column), and N2LO (right column) with corresponding 1σ (darker bands) and 2σ (lighter bands) error bands for $^{12}\mathrm{C}(n,n)^{12}\mathrm{C}$ at (first row) 65 MeV, (second row) 95 MeV, (third row) 155 MeV, and (fourth row) 185 MeV. Black dots are experimental data from Ref. [21]. See text for further discussion.

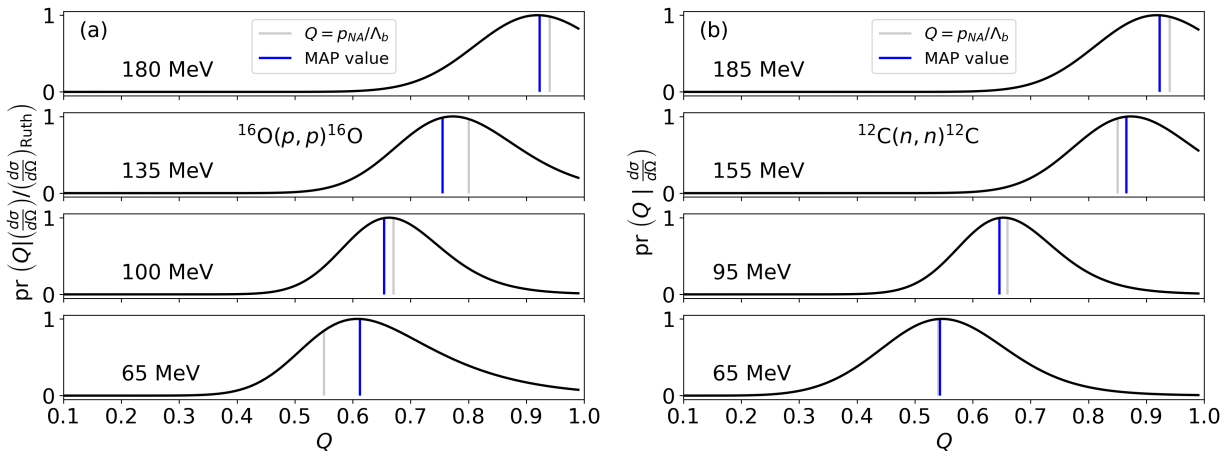


FIG. 4. Posterior plots for the expansion parameter Q given the calculated (a) differential cross section divided by Rutherford for ^{16}O$(p,p)^{16}$O and (b) differential cross section for ^{12}C$(n,n)^{12}$C. The single best guess from the posteriors (MAP value) is compared to an estimate based on our choice of the relevant momentum at various energies. See text for further discussion.

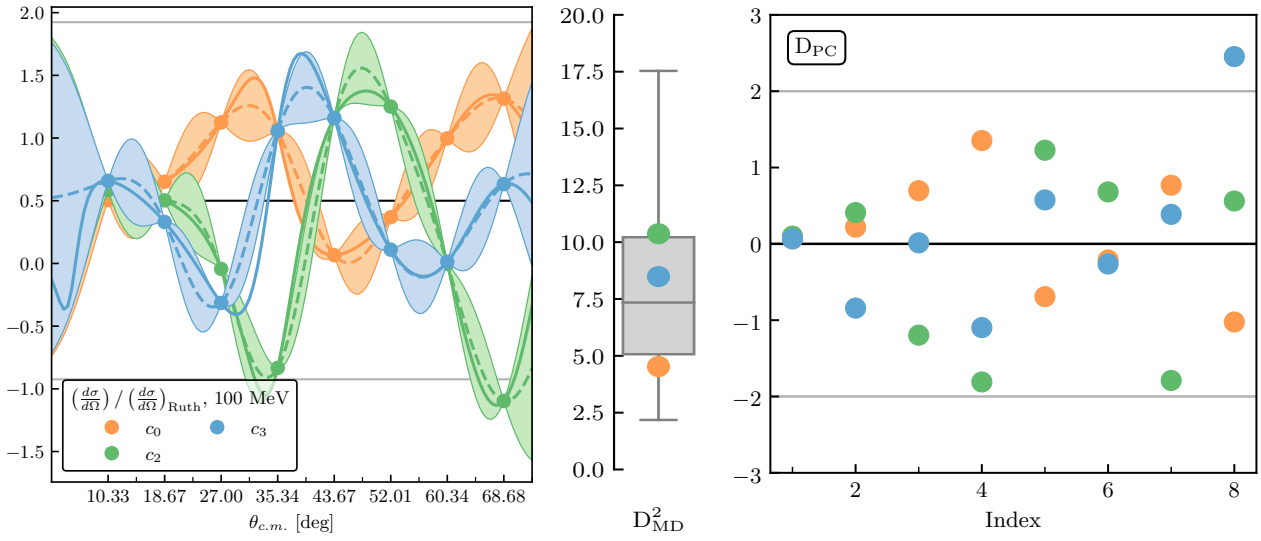


FIG. 5. Coefficient curves at each order and associated diagnostics for the differential cross section (divided by Rutherford) of ^{16}O$(p,p)^{16}$O at 100 MeV. For the coefficient curve plot, major tick marks on the x-axis represent training points and minor tick marks represent testing points for the Gaussian process. See text for further discussion.

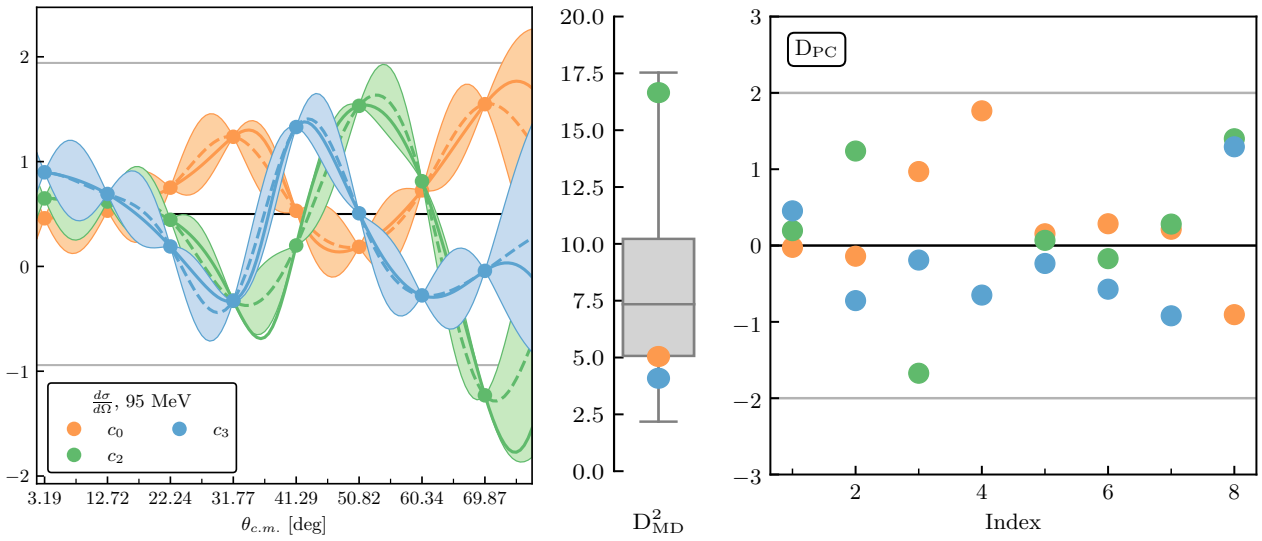


FIG. 6. Coefficient curves at each order and associated diagnostics for the differential cross section of $^{12}\mathrm{C}(n,n)^{12}\mathrm{C}$ at 95 MeV. For the coefficient curve plot, major tick marks on the x-axis represent training points and minor tick marks represent testing points for the Gaussian process. See text for further discussion.

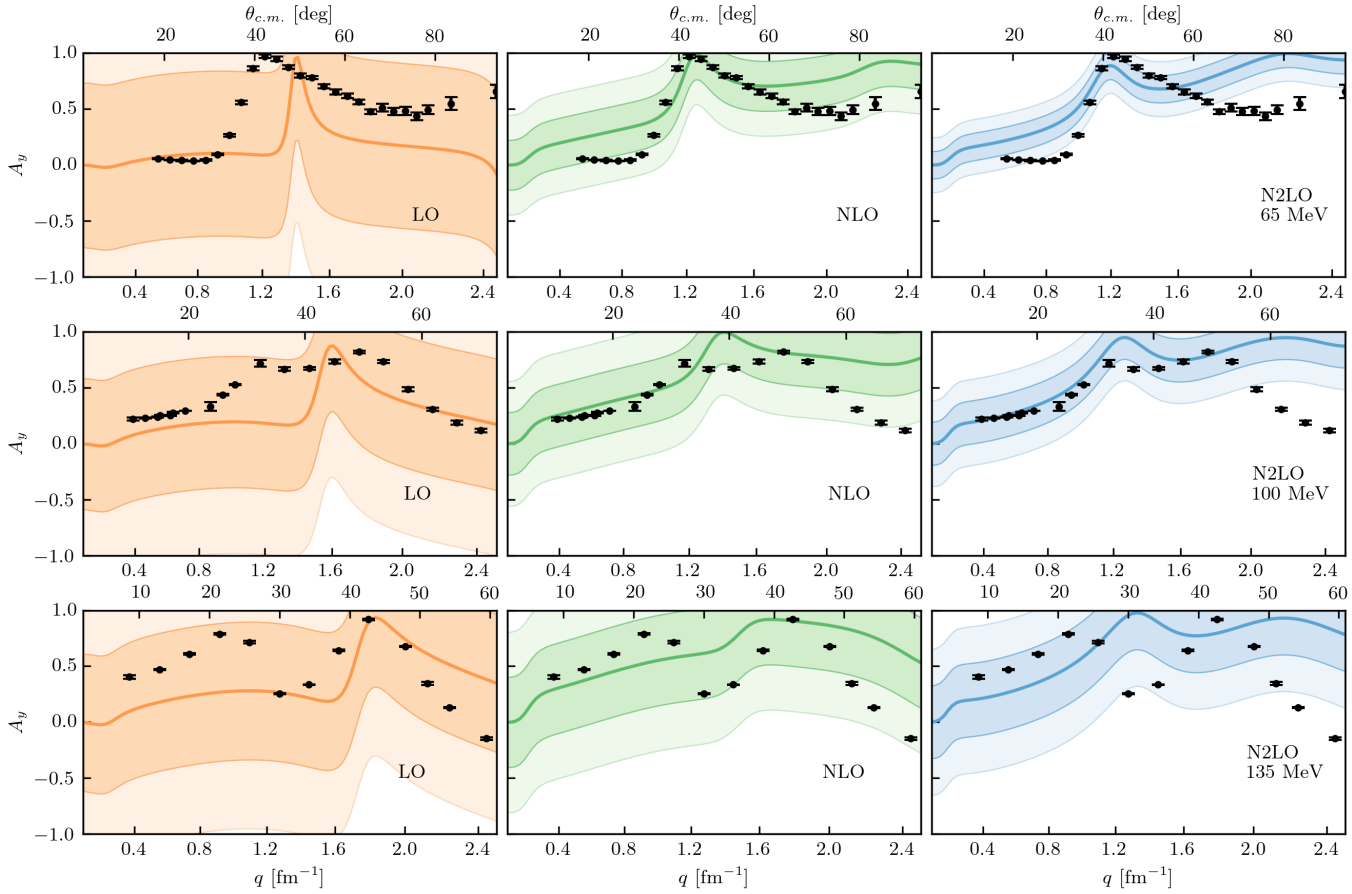


FIG. 7. Analyzing power at LO (left column), NLO (middle column), and N2LO (right column) with corresponding 1σ (darker bands) and 2σ (lighter bands) error bands for $^{16}\mathrm{O}(p,p)^{16}\mathrm{O}$ at (first row) 65 MeV, (second row) 100 MeV, and (third row) 135 MeV. Black dots are experimental data from Refs. [37] for 65 MeV, [38] for 100 MeV, and [39] for 135 MeV. See text for further discussion.

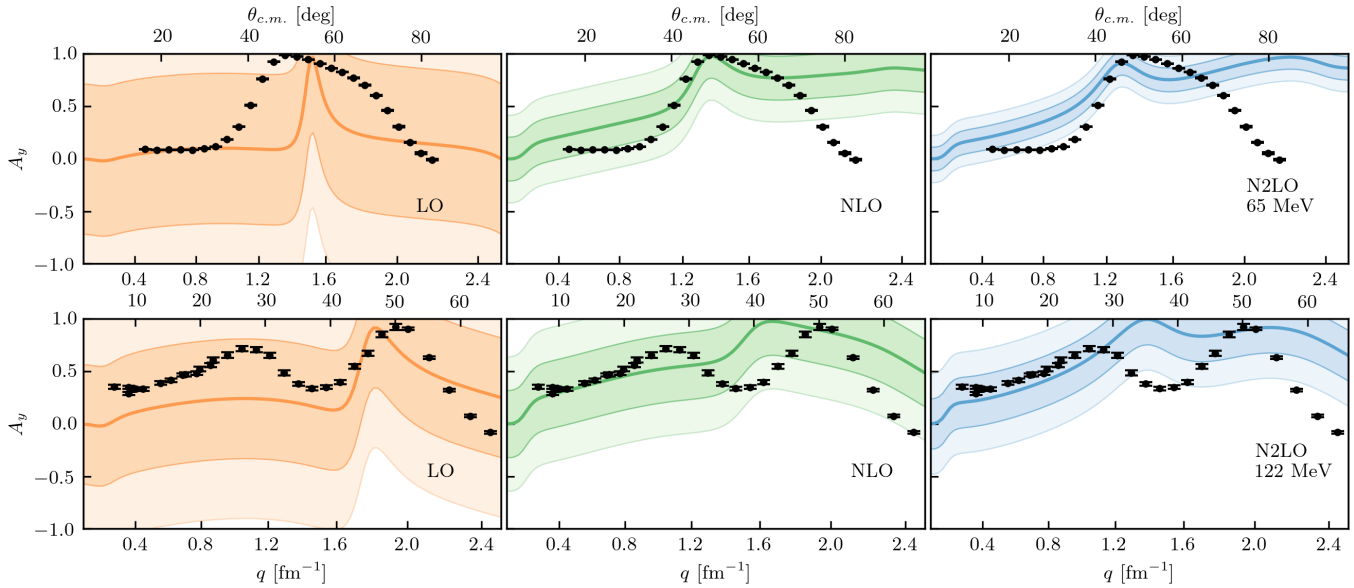


FIG. 8. Analyzing power at LO (left column), NLO (middle column), and N2LO (right column) with corresponding 1σ (darker bands) and 2σ (lighter bands) error bands for $^{12}\mathrm{C}(p,p)^{12}\mathrm{C}$ at (first row) 65 MeV and (second row) 122 MeV. Black dots are experimental data from Refs. [41] for 65 MeV and [42] for 122 MeV. See text for further discussion.

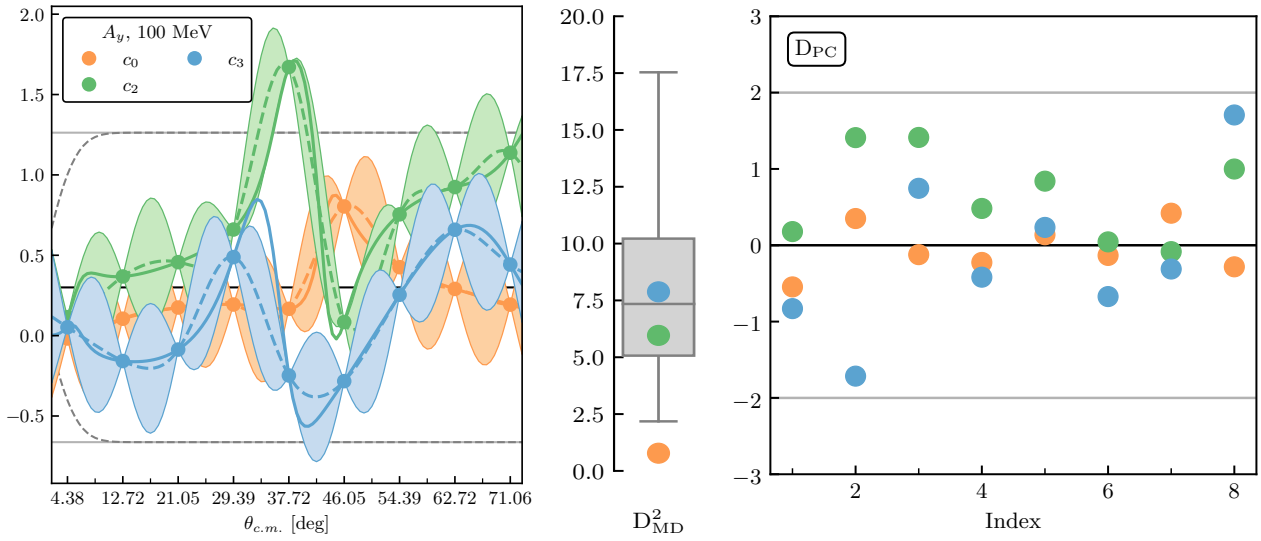


FIG. 9. Coefficient curves at each order and associated diagnostics for the analyzing power of $^{16}\mathrm{O}(p,p)^{16}\mathrm{O}$ at 100 MeV. For the coefficient curve plot, major tick marks on the x-axis represent training points and minor tick marks represent testing points for the Gaussian process. The gray dashed line indicates the constraint on the underlying distribution which requires the A_y (and the coefficients) to be 0 at 0°. See text for further discussion.

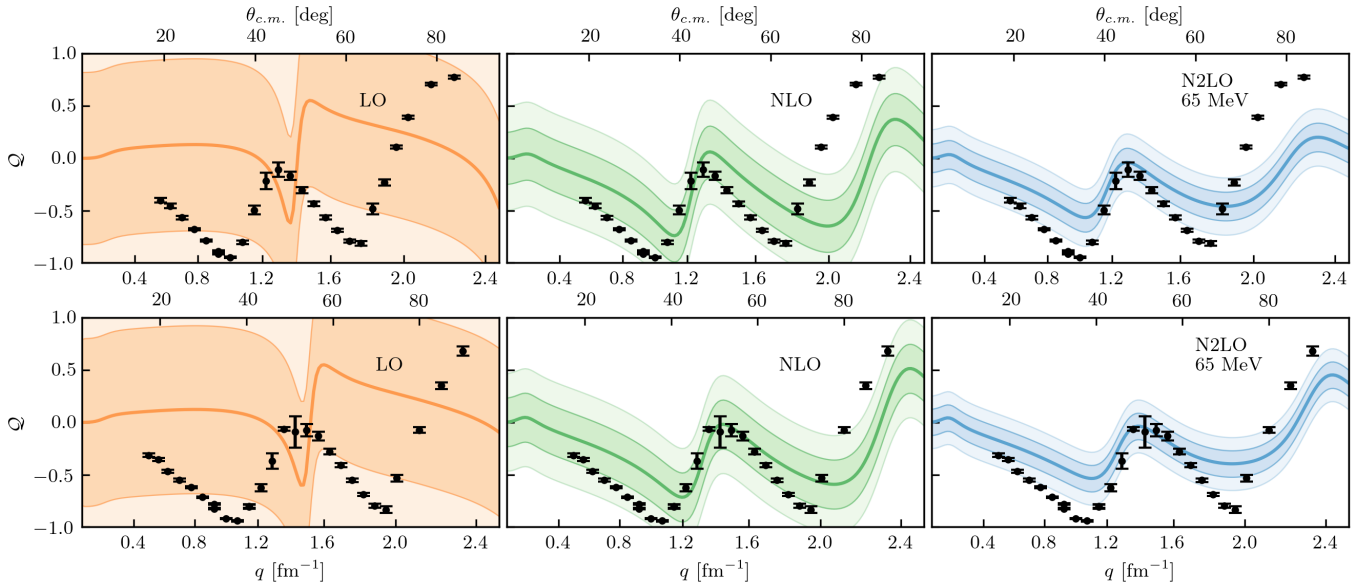


FIG. 10. Spin rotation function at LO (left column), NLO (middle column), and N2LO (right column) with corresponding 1σ (darker bands) and 2σ (lighter bands) error bands for (first row) $^{16}\mathrm{O}(p,p)^{16}\mathrm{O}$ and (second row) $^{12}\mathrm{C}(p,p)^{12}\mathrm{C}$, both at 65 MeV. Black dots are experimental data from Ref. [43]. See text for further discussion.

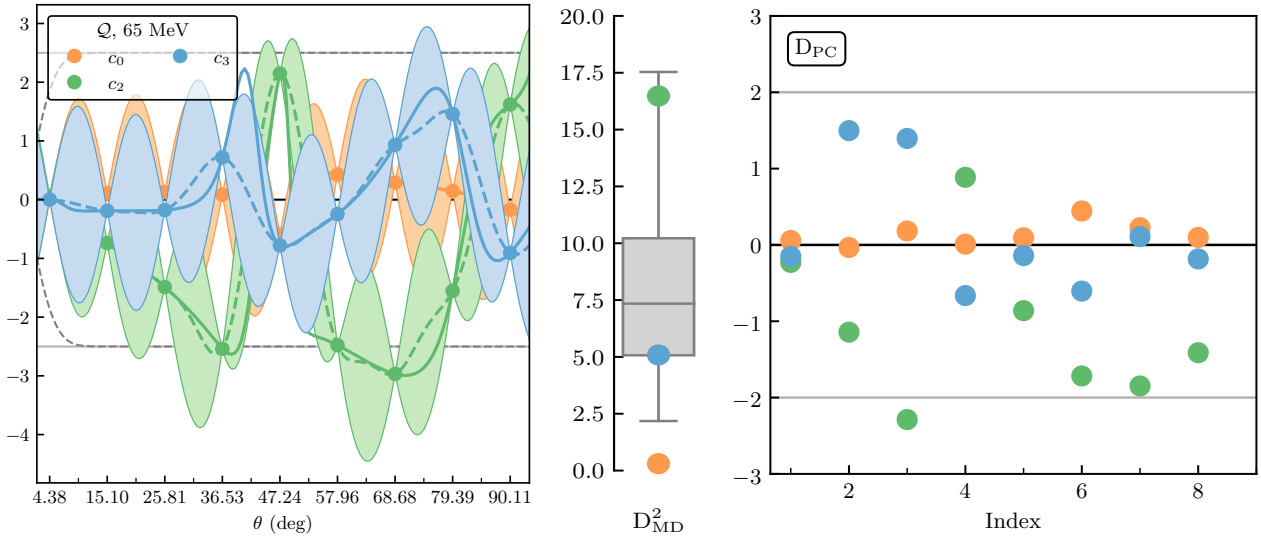


FIG. 11. Coefficient curves at each order and associated diagnostics for the spin rotation function of $^{16}\mathrm{O}(p,p)^{16}\mathrm{O}$ at 65 MeV. For the coefficient curve plot, major tick marks on the x-axis represent training points and minor tick marks represent testing points for the Gaussian process. The gray dashed line indicates the constraint on the underlying distribution which requires the $\mathcal{Q}$ (and the coefficients) to be 0 at 0°. See text for further discussion.

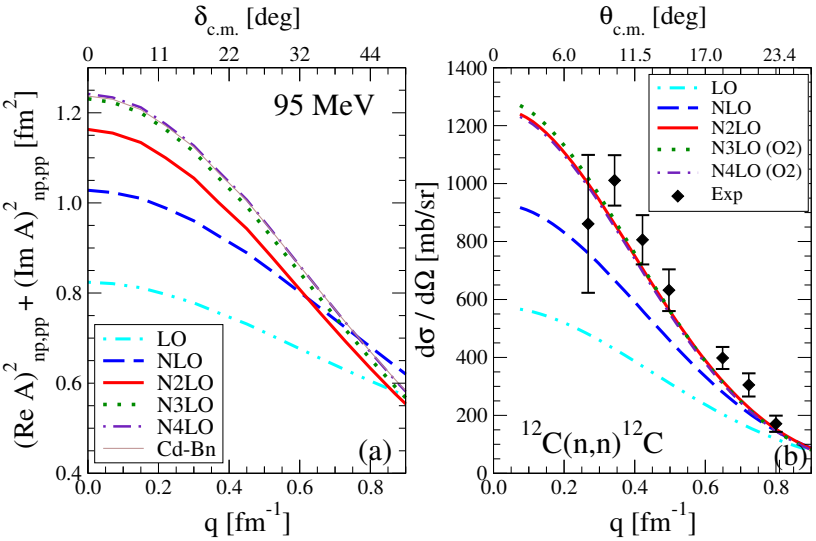


FIG. 12. (a) Wolfenstein amplitudes calculated at 95 MeV for various orders of the chiral NN interaction [2]. The result for the CD-Bonn potential [44] is shown for comparison. (b) The differential cross section for $^{12}\mathrm{C}(n,n)^{12}\mathrm{C}$ at 95 MeV calculated for the same orders. The black dots and error bars show experimental data from Ref. [21]. See text for further discussion.

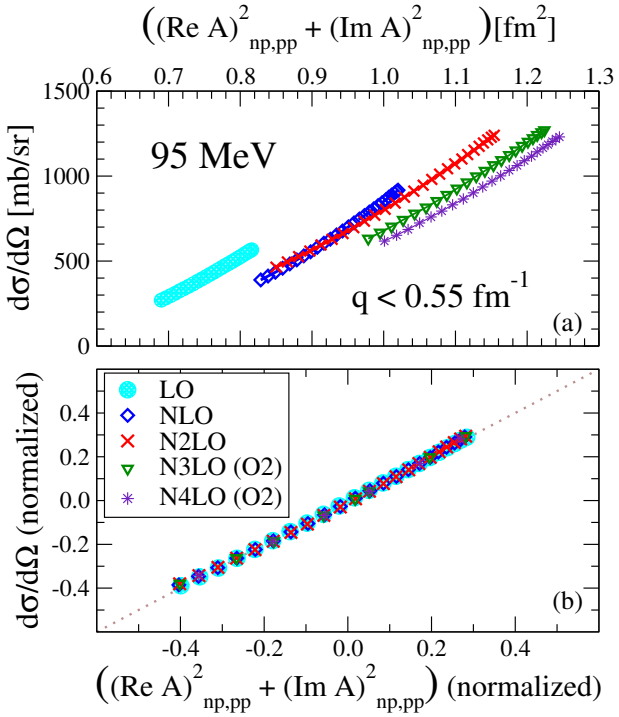


FIG. 13. (a) Differential cross section for $^{12}\mathrm{C}(n,n)^{12}\mathrm{C}$ as a function of Wolfenstein amplitudes, both at 95 MeV for the same orders as in Fig. 12, and for values of the momentum transfer less than 0.55 fm^{-1}. (b) Correlation plot of the same quantities as in (a), but normalized to illustrate the near perfect correlation, with a correlation coefficient of 0.99. The dotted gray line indicates a perfect positive correlation. See text for further discussion.